Int J Thermophys (2008) 29:2149–2161
DOI 10.1007/s10765-008-0421-1

In-depth and In-plane Thermal Diffusivity Measurements of Thermal Barrier Coatings by IR Camera: Evaluation of Ageing

P. Bison · F. Cernuschi · E. Grinzato

Published online: 9 April 2008
© Springer Science+Business Media, LLC 2008

Abstract Ceramic thermal barrier coatings (TBCs) are widely used for protecting hot path components from combustion gases in gas turbines for both aero- and land-based applications. TBCs undergo degradation and eventually detach from the substrate. Forecasting of the detachment of TBCs for timely maintenance is an open problem in gas turbine technology. It is known that sintering happens in the TBCs when exposed to high temperature. Sintering affects the mechanical properties of TBCs and mainly their strain compliance for which degradation causes the detachment. As sintering strongly affects the thermal diffusivity of TBCs also, the idea is to measure the latter parameter to account for the former. Pulsed thermography is the technique selected to monitor the thermal diffusivity variation due to TBC ageing. In perspective, it should be applied to monitor the gas turbine during the normal stop for maintenance. This article reports preliminary laboratory tests carried out on a set of metal samples coated with TBCs. The samples were aged during cyclic oxidation tests at various percentages of their estimated life, the end of life being the time of the TBC detachment from the substrate. The identification of the thermal diffusivity in the coating layer is carried out for the general case of anisotropic conductivity.

Keywords Thermal diffusivity measurement · Thermal barrier coating · Thermography

P. Bison (✉) · E. Grinzato
CNR-ITC, C.so Stati Uniti 4, 35127 Padova, Italy
e-mail: paolo.bison@itc.cnr.it

F. Cernuschi
CESI RICERCA, via Rubattino 54, 20134 Milano, Italy

1 Introduction

The gas turbine that is utilized in an aircraft and their land-based version applied in the power generation industry undergo stressing conditions in their hot path. The vanes, blades, transition pieces, and especially the combustion chambers are required to withstand temperatures close to the melting point. This is caused by the very high temperature of combustion gases. Moreover, corrosion and erosion effects occur due to both the combustion and the high velocity of gases.

For all these reasons, it is common to protect the metallic base material of the hot path components by depositing a refractory ceramic porous layer on the surfaces. The state-of-the-art of these ceramic thermal barrier coatings (TBCs) is represented by yttrium oxide partially stabilized zirconium (YPSZ) oxide (7–8% in mass of $Y_2O_3 + ZrO_2$) deposited onto components either by air plasma spray (APS) or by electron beam physical vapor deposition (EB-PVD) [1–3]. Depending on the TBC thickness and its specific thermal properties, the temperature of the metallic substrates can be reduced from 30°C to 100°C. The deposition process affects the microstructure of these coatings. As a consequence, the strain tolerance, erosion resistance, and the mechanical and thermophysical properties vary significantly [4–11].

Once exposed to the high temperature of the turbine engine, sintering takes place on TBCs modifying the mechanical and thermophysical properties. Both the microhardness and elastic modulus increase with sintering phenomena. This leads to a significant reduction of the strain compliance, and thus of the "life" of the TBCs, leading finally to the spallation of the protecting layer from the substrate.

Active thermography has been successfully applied to identify the disbonding of TBCs [12–15]. Here, active thermography is applied to monitor the TBC degradation. For this purpose a new line of investigation is followed: as sintering affects the mechanical properties of TBCs and their thermal properties as well, to account for the former the latter are measured. This approach potentially allows measurements to be carried out in situ, e.g., on power plants. In fact, thermal properties are more easily measured in situ, e.g., by contactless techniques like thermography. Due to the lack of a general theory that can be used to develop a correlation between mechanical and thermal properties in porous complex materials such as TBCs, an experimental relationship between mechanical and thermal properties, for various stages of sintering (ageing), should be established. This could be carried out by measuring independently the elastic modulus and thermal diffusivity of artificially aged samples.

The present work deals with the thermographic technique utilized to measure the thermal diffusivity of TBC coatings deposited on a metal substrate. The details and motivation for the choice of this technique, the thermal model, and some preliminary results have been reported elsewhere [16]. Here we stress the possibility to measure the two components of the anisotropic thermal diffusivity by using the data coming from one experiment. In fact, TBCs present different degrees of anisotropy, depending up on the deposition process. The technique consists of heating the surface of the sample (the TBC coatings deposited on the metal substrate) with a short pulse of light, spatially localized, and taking several images of the surface temperature evolution with an IR camera. The heat pulse diffuses in-depth (through the thickness of the coating)

and in-plane (spreading on planes parallel to the surface of the coating), modifying the surface temperature field that eventually can be used to evaluate the diffusivity.

2 Theory

A summary of the thermal model that describes the experiment and the obtained solution is given in the following. The domain consists of a plane layer (coating) with thickness l_c; α_P and α_N which are, respectively, the in-plane (parallel) and in-depth (normal) thermal diffusivities; λ_N is the normal thermal conductivity of the coating; and ε_C is the thermal effusivity of the coating. The coating is in contact with an isotropic substrate, considered semi-infinite, with diffusivity α_S and effusivity ε_S. No exchange with the environment is considered. A circular symmetry is assumed for the heating source, while its time dependence is represented by an ideal Dirac delta function. Hence, the heating function $H(r,t) = f(r)\delta(t)$ does not depend on the angle of the coordinate system (r,θ). See Fig. 1.

The temperature solution on the surface is obtained by using the technique of the integral transformation [16–18], and it is expressed in terms of the Fourier-Bessel transform in space Θ:

$$\Theta(k, z=0, t) = F(k)\mathrm{e}^{-\alpha_P k^2 t} L^{-1}\left[\frac{1}{\lambda_N q_N}\left[\frac{1+\Gamma_{3D}\mathrm{e}^{-2q_N l_c}}{1-\Gamma_{3D}\mathrm{e}^{-2q_N l_c}}\right]\right]$$

$$\Gamma_{3D} = \frac{\varepsilon_C - \varepsilon_S\sqrt{1+\frac{\Delta\alpha}{\alpha_N}\frac{k^2}{q_N^2}}}{\varepsilon_C + \varepsilon_S\sqrt{1+\frac{\Delta\alpha}{\alpha_N}\frac{k^2}{q_N^2}}} q_N = \sqrt{\frac{p}{\alpha_N}} \quad \Delta\alpha = \alpha_S - \alpha_P \tag{1}$$

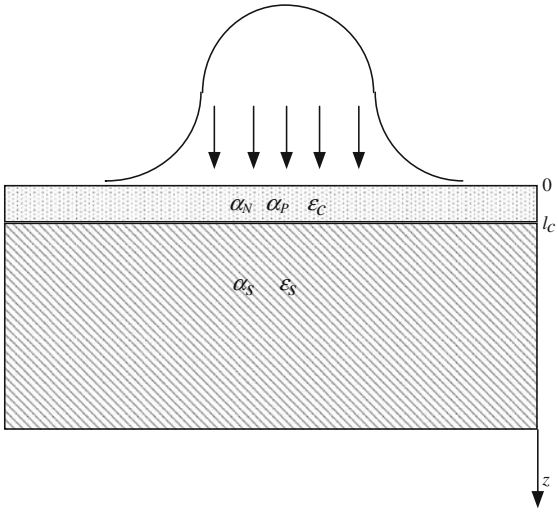

Fig. 1 Schematic diagram of the domain. Substrate is much thicker than the coating and is considered infinitely extended along the z-axis. On the accessible surface, a heat pulse is released with a spatially circular shape. Thermal diffusivity α and thermal effusivity ε indicate the thermal parameters for the two materials. Note the different *normal* and *parallel* values of the thermal diffusivity of coating

$F(k)$ is the Fourier-Bessel transform of $f(r)$ and k is the spatial frequency; L^{-1} is the inverse Laplace transform and p is the Laplace variable. A particularity of Eq. 1 is obtained when the zero frequency of the Fourier-Bessel variable is considered, viz., $k = 0$. In such a case, $\Gamma_{3D} \to \Gamma_{1D} = (\varepsilon_C - \varepsilon_S)/(\varepsilon_C + \varepsilon_S)$ and an explicit Laplace inversion is available for the expression indicated inside the square brackets of Eq. 1. Moreover, assuming $k = 0$ in Eq. 1 corresponds to spatial integration of the surface temperature [16]. From the definition of the Fourier-Bessel transform, where J_0 is the Bessel function of zero order, one obtains

$$\begin{aligned}\Theta(k=0,z=0,t) &= \frac{Q_0}{\varepsilon_C\sqrt{\pi\, t}}\left[1+2\sum_{n=1}^{\infty}\Gamma_{1D}^{n}\mathrm{e}^{-\frac{n^2 l_c^2}{\alpha_N t}}\right]\\ &= \frac{1}{2\pi}\int_0^{2\pi}\mathrm{d}\theta\int_0^{\infty} r\,J_0(0)T_C(r,z=0,t)\mathrm{d}r\\ &= \frac{1}{2\pi}\int_{-\infty}^{\infty}\int_{-\infty}^{\infty} T_C(x,y,z=0,t)\mathrm{d}x\,\mathrm{d}y \end{aligned} \tag{2}$$

where $T(x, y, z = 0, t)$ is the surface temperature field, t is the time, Q_0 is the total energy absorbed by the coating, and Γ_{1D} is the so-called mismatch coefficient between the coating and substrate. Equation 2 corresponds to the solution that one obtains when a spatially uniform pulse (instead of a localized one) heats the surface of the system, provided that Q_0 is interpreted as the specific energy.

This result states that even with a strongly spatially uneven source, the temperature field of the 1D case (uniformly heated sample, in-depth only heat diffusion) may be obtained by spatially integrating every IR image of the experiment. A nonlinear least-squares minimization of the data with Eq. 2 gives eventually the α_N/l_c^2 parameter together with Γ_{1D} and the multiplicative coefficient, $Q_0/\varepsilon_C\sqrt{\pi}$. The in-depth diffusivity α_N may be obtained once the thickness of the coating l_c is known. The thickness is determined in situ, e.g., by using an eddy current probe.

The measurement of the in-plane diffusivity can be determined using two approaches. The first is based on an important result as first pointed out by Philippi et al. [17]. Philippi et al. state that in a slab or semi-infinite body the spatial Fourier transform of the in-plane temperature field decays exponentially with time once normalized by its continuous component [20]:

$$\frac{\Theta(k,z,t)}{\Theta(k=0,z,t)} = \frac{F(k)}{F(k=0)}\mathrm{e}^{-\alpha_p k^2 t} \tag{3}$$

The time constant is proportional to the squared spatial frequency multiplied by the in-plane diffusivity. Hence, by taking the logarithm of the ratio given by Eq. 3 it is possible to obtain the in-plane diffusivity from the slope of the fitted straight line. Equation 3 is correct only for a homogeneous finite thickness slab or a homogeneous semi-infinite body, but not for a two-layer system like the one we are analyzing. It could be utilized only for very short times, immediately after the pulse, when the heat

front is still traveling in the coating (the first layer) and it has not yet reached the boundary with the substrate.

Alternatively, it is possible to use Eq. 1. In such a case, the time dependence of the spatial Fourier transform of the in-plane temperature field could be computed by the Stephest algorithm that gives a numerical inversion for the Laplace transform [19]. The spatial Fourier transform of the temperature data must be computed at every time and then used in a nonlinear fitting procedure to obtain the in-plane diffusivity. Note that many parameters needed in Eq. 1 are known from the in-depth diffusivity evaluation. Furthermore, the in-plane diffusivity estimation by Eq. 1 requires knowledge of the substrate diffusivity.

In the case of small k values (the spatial Fourier frequency), an expansion in a Taylor series could be done as shown in the following equation:

$$\begin{aligned}\Theta_{\mathrm{c}}(k, z=0, t) = F(k)\, \mathrm{e}^{-\alpha_{\mathrm{p}} k^2 t} \Bigg\{ & \frac{1}{\varepsilon_{\mathrm{C}}\sqrt{\pi t}} \left(1 + 2 \sum_{n=1}^{\infty} \Gamma_{1\mathrm{D}}^{n} \mathrm{e}^{-\frac{n^2 l_{\mathrm{c}}^2}{\alpha_{\mathrm{N}} t}} \right) \\ & - 4\,\Delta\alpha \frac{\gamma}{(1+\gamma)^2} \sum_{n=0}^{\infty} (n+1)\, \Gamma_{1\mathrm{D}}^{n} \cdot \Bigg[\frac{2}{\varepsilon_{\mathrm{C}}} \sqrt{\frac{t}{\pi}} \mathrm{e}^{-\frac{(n+1)^2 l_{\mathrm{c}}^2}{\alpha_{\mathrm{N}} t}} \\ & - (n+1)\, \frac{2}{\varepsilon_{\mathrm{C}}} \frac{l_{\mathrm{c}}}{\sqrt{\alpha_{\mathrm{N}}}} \mathrm{Erf}\left(\frac{(n+1)\, l_{\mathrm{c}}}{\sqrt{\alpha_{\mathrm{N}} t}} \right) \Bigg] \frac{k^2}{2!} + 0^4 \Bigg\} \end{aligned} \tag{4}$$

3 Numerical Simulations

A numerical simulation with a finite difference code [21] was carried out to test the capabilities of Eqs. 1–4 to determine the in-depth and in-plane thermal diffusivities. In the simulation, a two-layer system was considered with thermal properties and thicknesses typical of a real component to be inspected (e.g., a turbine blade). The uneven heating is spatially a Gaussian with a diameter (measured as full width at half maximum) of 0.0057 m, and in time, a square pulse of 1 ms duration. The main parameters used in the simulation are summarized in Table 1.

Figures 2 and 3 show the results obtained from the simulation data in Table 1 for TBC 1. Figure 2 shows the application of Eq. 2 to determine the in-depth diffusivity of the TBCs. Data (plotted with small circles) represent the spatial average temperature coming from the numerical simulation. The continuous line represents the interpo-

Table 1 Summary of the parameters of the finite difference numerical simulation for two APS TBCs

	TBC 1	TBC 2	Metal alloy substrate
In-plane thermal conductivity ($\mathrm{W \cdot m^{-1} \cdot K^{-1}}$)	1.175	1.438	10
In-depth thermal conductivity ($\mathrm{W \cdot m^{-1} \cdot K^{-1}}$)	0.94	1.678	10
Density ($\mathrm{kg \cdot m^{-3}}$)	5000	5100	8400
Specific heat ($\mathrm{J \cdot kg^{-1} \cdot K^{-1}}$)	470	470	440
Thickness (mm)	0.350	0.350	3.0

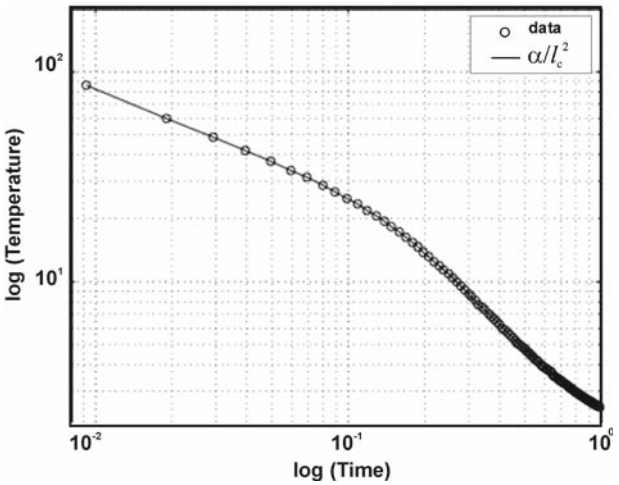

Fig. 2 Log–log representation of the spatial integral of the surface temperature. Data refer to the numerical simulation results obtained by the finite difference method. Legend reports the estimated parameter α/l^2 involved in the in-depth heat propagation and obtained by a nonlinear fit of the data using Eq. 2

lating function that fits the data. This plot shows, on a log–log scale, the behavior of the specimen. Near the beginning of the process, when the heat front has not yet reached the boundary with the substrate, the TBC coating is sensed as a semi-infinite body (-0.5 slope of the straight line). After that, we notice a transition zone. Finally, the data follows again a straight line of slope -0.5. At this point, the heat front has reached the semi-infinite body represented by the substrate.

Figure 3 shows the application of Eq. 3 to determine the in-plane diffusivity. Data represent the logarithm of the ratio between the discrete cosine transform of the surface temperature relative to the II, IV, VI frequency components and the zeroth component. Data are given as a function of time. It is interesting to note how these data bend after an initial phase. That is due to the inhomogeneity of the system. For the case of a homogeneous slab or semi-infinite body, these curves are straight lines. To obtain a good estimation of the thermal diffusivity by using Eq. 3, we must restrict the data for analysis, as stated later at point (c). The time limit can be inferred by examining the in-depth analysis of Fig. 2. The limiting time must be chosen in the first part of the curve, before the bending from the slope -0.5, which means, for the case represented in Fig. 2, around 50 ms.

From the simulation and the application of the Eqs. 1–4 to determine the thermal diffusivity, we obtained the following results:

(a) The application of Eq. 2 for the in-depth diffusivity determination seems to work generally well.
(b) The straightforward application of Eq. 1 and/or Eq. 4 to determine the in-plane diffusivity with a nonlinear minimization procedure does not give good results. Such formulae seem to have a very poor sensitivity to the diffusivity variation.
(c) To determine the in-plane diffusivity, it is therefore necessary to use Eq. 3, limiting the data used in the fit to a short time interval, immediately after the heating

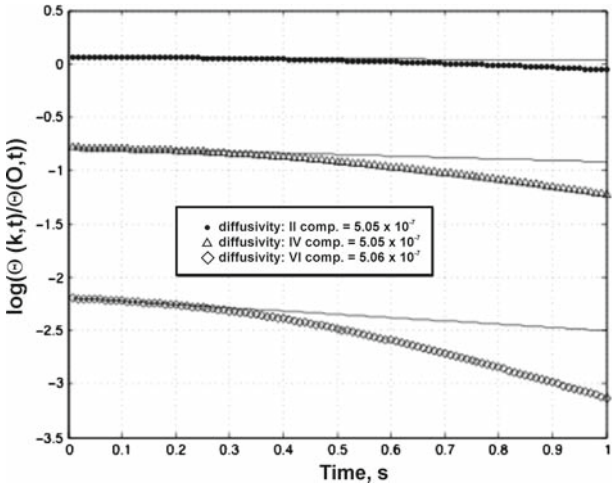

Fig. 3 Spatial discrete cosine transform (DCT) of the surface temperature for each time step of the numerical simulation by the finite difference method. Three components with the highest amplitude are shown. Logarithm of the data is linearly fitted according to Eq. 3, considering only the first part of the curves, when the heat front is still traveling in the coating layer. Legend shows the values obtained for the estimated in-plane diffusivity

pulse. This time interval must be limited to the traveling time of the heat front from the surface to the substrate interface. When this condition is met, Eq. 3 gives generally good results.

4 Uncertainty Analysis

The uncertainty of the estimated in-depth and in-plane diffusivities are given applying the general rules of uncertainty analysis [22–24] and considering the implementation of algorithms such as fast Fourier transform (FFT), discrete cosine transform (DCT), covariance, and linear least-squares fits [25].

The temperature measured in each pixel is assumed to be affected by noise with a Gaussian distribution, characterized by a zero mean value and standard deviation σ. Noise affecting one pixel temperature at time t is assumed to be uncorrelated to that of any other pixel. The same is assumed for the noise affecting one pixel temperature at different times. The standard deviation σ can be inferred from the camera characteristics. Alternatively, σ can be computed for an image, which is assumed to be at a uniform temperature.

(a) The in-depth thermal diffusivity is obtained by Eq. 2. The surface temperature is integrated (actually averaged) in a suitable area for each IR image, i.e., for each time step of the acquisition. The result is a temperature profile in time. Assuming that the averaged area is a rectangle with N_x and N_y pixels for the horizontal and vertical sides, respectively, each averaged temperature is characterized by a standard deviation of

$$\sigma_A = \frac{\sigma}{\sqrt{N_x N_y}}$$

As described in the previous section, the unknown parameters are estimated by a nonlinear fitting procedure. When the optimization algorithm reaches the minimum of the cost function (in the specific case, the χ^2), the set of parameters $\mathbf{P}$, defined as

$$\mathbf{P} = \begin{bmatrix} p_1 & p_2 & p_3 \end{bmatrix} = \begin{bmatrix} \frac{Q_0}{\varepsilon_C \sqrt{\pi}} & \frac{\alpha_N}{l_c^2} & \Gamma_{1D} \end{bmatrix}$$

is optimum. For this optimum combination of the parameters $\mathbf{P}_{opt}$, the Jacobian matrix of the model function (Eq. 2) is computed:

$$\mathbf{J} = \begin{bmatrix} \partial f(\mathbf{P}_{opt}, t_1)/\partial p_1 & \partial f(\mathbf{P}_{opt}, t_1)/\partial p_2 & \partial f(\mathbf{P}_{opt}, t_1)/\partial p_3 \\ \cdots & \cdots & \cdots \\ \partial f(\mathbf{P}_{opt}, t_{N_t})/\partial p_1 & \partial f(\mathbf{P}_{opt}, t_{N_t})/\partial p_2 & \partial f(\mathbf{P}_{opt}, t_{N_t})/\partial p_3 \end{bmatrix}$$

where t_i ($i = [1{:}N_t]$) are the time steps of the acquisition process.

The uncertainties of the parameters are formally given by the covariance matrix according to the following equation:

$$\mathrm{cov}(\mathbf{P}_{opt}) = \sigma_A^2 (\mathbf{J}' \cdot \mathbf{J})^{-1} = \begin{bmatrix} \sigma_{p_1}^2 & \sigma_{p_1,p_2}^2 & \sigma_{p_1,p_3}^2 \\ \sigma_{p_2,p_1}^2 & \sigma_{p_2}^2 & \sigma_{p_2,p_3}^2 \\ \sigma_{p_3,p_1}^2 & \sigma_{p_3,p_2}^2 & \sigma_{p_3}^2 \end{bmatrix}$$

where the diagonal elements of the matrix correspond to the variances of the parameters, and the off-diagonal elements are the covariances.

Finally, the uncertainty expression for the in-depth diffusivity is given by

$$\frac{\sigma_{\alpha_N}}{\alpha_N} = \frac{\sigma_{p_2}}{p_2} + 2\frac{\Delta l_c}{l_c}$$

where Δl_c is the uncertainty related to the measurement of the coating thickness.

(b) For the in-plane thermal diffusivity evaluation, the first step in our data reduction procedure is the integration of temperature along one dimension, say x. The corresponding standard deviation of the integrated temperature is

$$\sigma_I = \sqrt{N_x}\sigma$$

where N_x is the number of integrated pixels. On the other hand, the averaging of temperature, instead of integration, leads to a correct answer as well. The averaging of temperature introduces just a scaling factor of $1/N_x$ in the temperature signal. The standard deviation of the mean value is given by

$$\sigma_A = \frac{\sigma}{\sqrt{N_x}}$$

At this stage, the Fourier transform or cosine transform is applied to the array of temperature obtained in the previous step. The problem now is: given a spatial profile of temperatures affected by noise, with a known standard deviation, what is the value

of the standard deviation in the Fourier transformed vector? The theory affirms that it is the same, because the norm of the vector in the direct and transformed space is conserved by virtue of Parseval's identity. In practice, one should pay attention to the practical implementation of the transformation algorithm, and especially to the normalization used. For example, using the algorithms for the covariance, fast Fourier transform, discrete cosine transform, and random generator for Gaussian noise, one can produce a known signal, replicate it N times, and add to each replicate a different realization of noise with the same standard deviation, say σ. Computing the covariance in the direct space, one obtains a matrix with a diagonal (the variance of the noise) whose value fluctuates around σ^2. Off-diagonal values (covariances) are around zero, meaning that the noise is uncorrelated. In the transformed space, the covariance matrix gives essentially the same value (σ^2) for the DCT and N times that value for FFT ($N\sigma^2$), with N being the signal dimension (number of pixels). What depends on the normalization factor in the DCT is $1/\sqrt{N}$, while no normalization is present in the FFT.

In our data reduction procedure, DCT is used and the standard deviation attributed to the transformed signal remains therefore equal to σ_{A}. Then, the logarithm of the ratio between the nth and zeroth components is computed. The uncertainty propagation leads to a standard deviation for the obtained values that depends on the amplitude of the cosine transformed signals:

$$\sigma_{\log}(k_n, t) = \sigma_{\mathrm{A}} \sqrt{\frac{1}{\Theta(k_n, t)^2} + \frac{1}{\Theta(0, t)^2}} = \frac{\sigma}{\sqrt{N_x}} \sqrt{\frac{1}{\Theta(k_n, t)^2} + \frac{1}{\Theta(0, t)^2}}$$

Next, the linear least-squares fit is implemented. The linear problem may be expressed in terms of a design (model) matrix **M**, the parameter vector **P** to be estimated, and the data vector **D** as follows:

$$\begin{bmatrix} 1/\sigma_{n,1} & t_1/\sigma_{n,1} \\ 1/\sigma_{n,2} & t_2/\sigma_{n,2} \\ \vdots & \vdots \\ 1/\sigma_{n,N_t} & t_{N_t}/\sigma_{n,N_t} \end{bmatrix} \cdot \begin{bmatrix} p_a \\ p_b \end{bmatrix} \approx \begin{bmatrix} d_{n,1}/\sigma_{n,1} \\ d_{n,2}/\sigma_{n,2} \\ \vdots \\ d_{n,N_t}/\sigma_{n,N_t} \end{bmatrix} \leftrightarrow \mathsf{M} \cdot \mathsf{P} \approx \mathsf{D}$$

$$\begin{cases} \sigma_{n,i} = \sigma_{\log}(k_n, t_i) \\ d_{n,i} = \log\left(\frac{\Theta(k_n, t_i)}{\Theta(0, t_i)}\right) \end{cases} \qquad i = [1 : N_t]$$

where N_t is the number of samples, $p_a = c(k_n)$ the intercept of the straight line, and $p_b = \alpha_{\mathrm{P}} k_n^2$ is the slope. Notice that each term in the design matrix **M** is weighted by the respective standard deviation, as the corresponding datum in the column vector **D**. Generally, N_t is much greater than two (the number of unknowns). Therefore, the linear system is overdetermined and it may be solved in the least-squares sense in terms of the 'normal equation' by the following relation:

$$\mathbf{P} = \left(\mathbf{M}' \cdot \mathbf{M}\right)^{-1} \cdot \mathbf{M}' \cdot \mathbf{D}$$

where the prime stands for matrix transposition.

For uncertainty analysis purposes, the covariance matrix of the obtained parameters is given by

$$\operatorname{cov}(\mathbf{P}) = \left(\mathbf{M}' \cdot \mathbf{M}\right)^{-1} \quad \operatorname{cov}(\mathbf{P}) = \begin{pmatrix} \sigma^2_{p_a} & \sigma^2_{p_a,p_b} \\ \sigma^2_{p_b,p_a} & \sigma^2_{p_b} \end{pmatrix}$$

Once p_b is computed, the diffusivity is determined if the spatial frequency is known. This implies a pixel calibration, i.e., the determination of the area viewed by the pixel in the real object. The pixel calibration and its uncertainty are often forgotten in the data analysis of the in-plane diffusivity evaluation by thermography. Without its specification, some authors report a value of around 0.15% for the uncertainty of the diffusivity measurement, which, in our opinion is too small for the actual uncertainty of such a technique.

Let us assume that the object under test is of length L, and its length in the thermographic image covers something like 100 pixels. The pixel calibration is therefore, $L/100$. The estimation of the number of pixels corresponding to the length of the object is not simple, as the edges in the thermographic image do not appear as sharp as in a visible band image. Therefore, one may estimate a relative uncertainty of approximately 2% corresponding to an estimation of the length of (100 ± 2) pixels.

Neglecting the covariances in the previous step, the final formula is therefore,

$$\frac{\sigma_{\alpha_\mathrm{P}}}{\alpha_\mathrm{P}} = \frac{\sigma_{p_b}}{p_b} + 2\frac{\sigma_{\Delta x}}{\Delta x}$$

The high pixel number of a thermographic sequence permits remarkable data reduction both in space and time. The first term in the last uncertainty propagation formula is generally much lower than the uncertainty introduced by the pixel calibration. We may state that a reasonable figure for the uncertainty in the in-plane thermal diffusivity measurement is $\geq$4%. We will see from the experimental data that the analysis above is optimistic.

5 Results

The experimental studies have been performed on a set of three pseudo-columnar APS TBC samples. The pseudo-columnar APS TBC is an evolution of the conventional APS TBC. In fact, due to the presence of regularly spaced in-depth cracks, as shown in Fig. 4, the TBCs exhibit a significant increase of the strain compliance with respect to the APS coatings. The pseudo-columnar TBCs are usually characterized by an overall porosity lower than that of conventional APS TBCs (values of 6–10% and 8–20% are typical for the latter and the former, respectively). Furthermore, in a conventional APS TBC, a significant portion of the porosity consists of lamellar-shaped pores oriented parallel to the surface, while the porosity of pseudo-columnar coatings consist mainly of in-depth cracks and a lower content of lamellar-shaped pores. Three samples are considered. The first is in the as-sprayed condition. The second and the third are

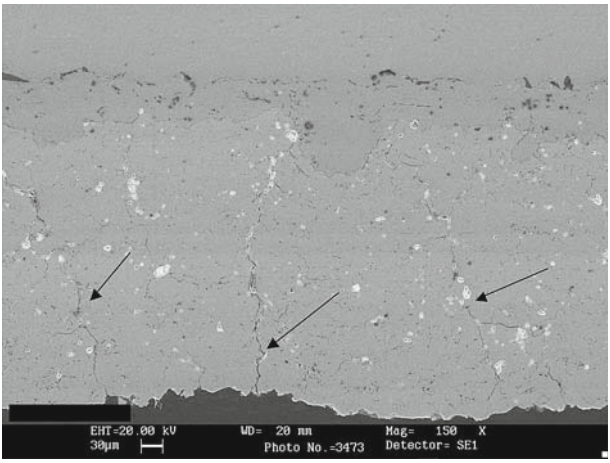

Fig. 4 Scanning electron microscopy image of an as-sprayed pseudo-columnar APS TBC. Typical through-the-thickness cracks perpendicular to the interface are clearly visible (as indicated by arrows)

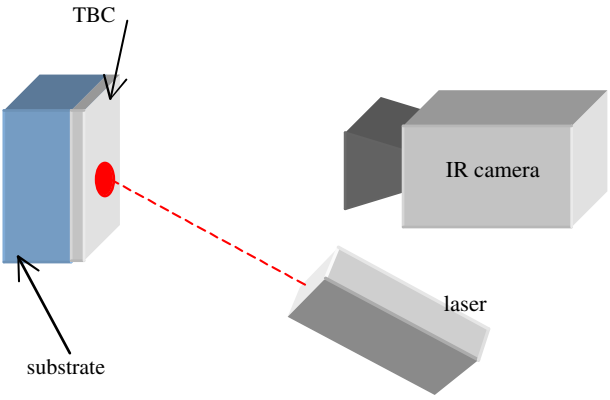

Fig. 5 Experimental setup. Pulsed laser heats the TBC specimen. IR camera used to obtain a sequence of images of the specimen surface temperature

aged up to 35% and 70% of their life by high-temperature cycles. The end of life is defined as the number of cycles needed for spalling the TBC from the substrate.

In the experimental setup, a laser (1,064 nm wavelength) generates a pulse of about 0.8 ms that heats the specimen surface on a circular area with a diameter of 10 mm. An IR camera is used to obtain a sequence of thermograms of the specimen surface at a frame rate of 150 Hz (as shown in the schematic in Fig. 5).

Results are reported in Table 2. Uncertainties are computed by simple mean and standard deviation computations on several tests carried out on each sample. While the results for the in-depth diffusivity show an error of approximately 5%, larger errors are obtained for the in-plane measurement. The in-plane measurements are more affected by the choice of the area where the spatial transform is computed and by the spatial resolution of pixels in the IR image. As a consequence, different values of the in-plane

Table 2 Results for the in-depth and in-plane thermal diffusivities of APS TBC

	α_N ($m^2 \cdot s^{-1}$)	α_P ($m^2 \cdot s^{-1}$)
TBC as-sprayed	4.91×10^{-7} ±3.8%	4.70×10^{-7} ±9.3%
TBC 35% of its life	7.05×10^{-7} ±5.2%	6.01×10^{-7} ±24%
TBC 70% of its life	6.08×10^{-7} ±5.4%	5.76×10^{-7} ±12%

diffusivity are obtained at different spatial frequencies and among different tests. The role of the parameters affecting the spatial transform computation (i.e., spatial window dimension, location of the window with respect to the heating zone, spatial resolution of the pixel) is beyond the scope of this work, but should be investigated in more depth in the future.

Concerning the results obtained as confirmation of data reported in Ref. [16], the in-depth diffusivity reflects a rapid increase of sintering in the first part of the TBC life. After that, a small decrease of the diffusivity is observed as a consequence of the formation of microcracks mainly close to the substrate interface.

By taking into account the aforementioned microstructural features of a pseudo-columnar APS TBC, it is possible to qualitatively explain the results also in comparison to those reported in Ref. [16], where conventional APS TBCs are considered. In particular, a slightly higher in-depth thermal diffusivity for the as-sprayed sample is observed for the pseudo-columnar TBC because of its more dense structure, with respect to that for a conventional TBC. A similar increase of the in-depth thermal diffusivity as a function of ageing is observed because both TBCs have been similarly affected by the sintering phenomena taking place at high temperature (the in-depth thermal diffusivity measurement is mainly sensitive to the healing of lamellar-shaped pores, parallel to the surface). Moreover, the anisotropy of the thermal diffusivity for pseudo-columnar TBCs is more evident going from the as-sprayed sample to the aged ones because the high-temperature exposure promotes mostly sintering of lamellar-shaped pores than for in-depth cracks that are wide enough not to close or partially heal. Similar arguments can be used to explain the smaller decrease of α_P with respect to α_N for the sample aged up to 70% (the vertical cracks that are not closed sufficiently maintain the in-plane strain compliance of the coating).

6 Conclusion

A methodology to assess in situ the residual life of TBCs is proposed. Mathematical modeling contributes both to simplify the experimental scheme and to identify the diffusivity variations of TBCs with ageing (sintering) phenomena. Preliminary results are reported on specimens of pseudo-columnar APS TBCs at various stages of their operating life for both in-depth and in-plane diffusivities.

Acknowledgment This work has been financed by the Research Fund for the Italian Electrical System under the Contract Agreement between CESI RICERCA and the Ministry of Economic Development—

General Directorate for Energy and Mining Resources stipulated on June 21, 2007 in compliance with the Decree n.73 of June 18, 2007.

References

1. V.P. Swaminathan, N.S. Cheruvu, in *Advanced Materials and Coatings for Combustion Turbines*, ed. by V.P. Swaminathan, N.S. Cheruvu (ASM International, Materials Park, Ohio, 1994)
2. W. Beele, G. Marijnissen, A. Van Lieshout, Surf. Coat. Technol. **120–121**, 61 (1999)
3. J.R. Nicholls, R. Wing, in *Proceedings of the Materials for Advanced Power Engineering 2002*, ed. by J. Lecomte-Beckers, M. Carton, F. Schubert, P.J. Ennis (Schriften des Forschungszentrum Julich, Liege, Belgium, 2002), pp. 449–463
4. S. Leigh, C.C. Berndt, J. Am. Ceram. Soc. **82**, 17 (1999)
5. J. Ilavsky, G.G. Long, A.J. Allen, C.C. Berndt, Mater. Sci. Eng. **A272**, 215 (1999)
6. R. Dutton, R. Wheeler, K.S. Ravichandran, K. An, J. Thermal Spray Technol. **9**, 204 (2000)
7. J.A. Thompson, T.W. Clyne, Acta Mater. **49**, 1565 (2001)
8. R. McPherson, Surf. Coat. Technol. **39/40**, 173 (1989)
9. D. Zhu, R.A. Miller, B.A. Nagaraj, R.W. Bruce, Surf. Coat. Technol. **138**, 1 (2001)
10. P. Scardi, M. Leoni, F. Cernuschi, A. Figari, J. Am. Ceram. Soc. **84**, 827 (2001)
11. F. Cernuschi, L. Lorenzoni, S. Ahmaniemi, P. Vuoristo, T. Mäntylä, J. Europ. Ceram. Soc. **25**, 393 (2005)
12. J.W. Maclachlan Spicer, W.D. Kerns, L.C. Aamodt, J.C. Murphy, J. Nondestruct. Eval. **8**, 107 (1989)
13. F. Cernuschi, E. Colombo, V. Russo, A. Salerno, S. Ghia, R. Marchesi, in *Proceedings of the 4th EURO-CERAMICS, vol. 9, Coatings and Joinings*, ed. by B.S.Tranchina, A. Bellosi, Rimini (1995), pp. 419–428, Gruppo Editoriale Faenza Editrice ISBN 88-8138-013-7
14. M. Oksanen, P. Fenici, A. Salerno, J. Varis, F. Cernuschi, in *Review of Progress in Quantitative Non Destructive Evaluation*, vol. 15, ed. by D.O. Thompson, D.E. Chimenti (Plenum Press, New York, 1995), ISBN 0-306-45310-X
15. F. Cernuschi, U. Netzelmann, K.J. Pohl, in *Proceedings of the Materials for Advanced Power Engineering 1998*, ed. by J. Lecomte, F. Schubert, P.J. Ennis (Schriften des Forschungszentrum Julich, Liège, Belgium, 1998), pp. 1449–1458
16. P.G. Bison, F. Cernuschi, E. Grinzato, S. Marinetti, D. Robba, Infrared Phys. Technol. **49**, 286 (2007)
17. I. Philippi, J.C. Batsale, D. Maillet, A. Degiovanni, Rev. Sci. Instrum. **66**, 182 (1995)
18. D. Maillet, S. André, J.C. Batsale, A. Degiovanni, C. Moyne, *Thermal Quadrupoles* (Wiley & Sons, New York, 2000)
19. H. Stehfest, Commun. ACM **13**, 47 (1970)
20. P.G. Bison, E. Grinzato, S. Marinetti, Quant. Infrared Thermogr. (QIRT) J. **1**, 241 (2004)
21. ThermoCalc-3D, Innovation Inc., Russia (1998)
22. P.R. Bevington, D.K. Robinson, *Data Reduction and Error Analysis for the Physical Sciences* (McGraw-Hill, New York, 1992)
23. W.H. Press, S.A. Teukolsky, W.T. Vetterling, B.F. Flannery, *Numerical Recipes in C* (Cambridge University Press, 1992)
24. B.N. Taylor, C.E. Kuyatt, NIST Tech. Note 1297 (1994)
25. MATLAB®, The Mathworks Inc., http://www.mathworks.com